**Geomechanics and Engineering**, *Vol. 38, No. 1 (2024) 29-44*
https://doi.org/10.12989/gae.2024.38.1.029

# Automated ground penetrating radar B-scan detection enhanced by data augmentation techniques

Donghwi Kim[a], Jihoon Kim[b] and Heejung Youn*

*Department of Civil and Environmental Engineering, Hongik University, 94, Wausan-ro, Mapo-gu, Seoul, Republic of Korea*

(*Received December 31, 2023, Revised June 19, 2024, Accepted June 21, 2024*)

**Abstract.** This research investigates the effectiveness of data augmentation techniques in the automated analysis of B-scan images from ground-penetrating radar (GPR) using deep learning. In spite of the growing interest in automating GPR data analysis and advancements in deep learning for image classification and object detection, many deep learning-based GPR data analysis studies have been limited by the availability of large, diverse GPR datasets. Data augmentation techniques are widely used in deep learning to improve model performance. In this study, we applied four data augmentation techniques (geometric transformation, color-space transformation, noise injection, and applying kernel filter) to the GPR datasets obtained from a testbed. A deep learning model for GPR data analysis was developed using three models (Faster R-CNN ResNet, SSD ResNet, and EfficientDet) based on transfer learning. It was found that data augmentation significantly enhances model performance across all cases, with the mAP and AR for the Faster R-CNN ResNet model increasing by approximately 4%, achieving a maximum mAP (Intersection over Union = 0.5:1.0) of 87.5% and maximum AR of 90.5%. These results highlight the importance of data augmentation in improving the robustness and accuracy of deep learning models for GPR B-scan analysis. The enhanced detection capabilities achieved through these techniques contribute to more reliable subsurface investigations in geotechnical engineering.

**Keywords:** B-scan; data augmentation; deep learning; ground-penetrating radar; object detection

## 1. Introduction

Ground-penetrating radar (GPR) technology has become an increasingly popular technique for geotechnical engineers as a non-destructive method for subsurface investigations. It uses high-frequency electromagnetic (EM) waves to penetrate the ground and measures wave reflection or attenuation. This information can then be used to create detailed images of the subsurface, showing the location and depth of various features, such as buried utilities, voids, fractures, and changes in soil or rock type (Baker *et al.* 2007, Persico 2014, Utsi 2017). Due to its ability to efficiently and accurately image the subsurface, its practicality has been evidenced by its widespread application in numerous studies and projects to understand underground conditions better. Civil engineering fields that use GPR include foundations (Çelik 2015, Tallini *et al.* 2004), tunnels (Alani and Tosti 2018, Feng *et al.* 2018, Lin *et al.* 2020), excavation broken zone (Yang *et al.* 2020), underground utilities (Chun *et al.* 2023, Kouros *et al.* 2018, Tanoli *et al.* 2019, Yuan *et al.* 2018), underground voids (Kong *et al.* 2018, Lai *et al.* 2017, Luo and Lai 2020, Yang *et al.* 2020), and bridges (Benedetto 2013, Benedetto *et al.* 2012). From a geotechnical perspective, GPR can provide unseen subsurface information for underground structures. It is also useful for identifying potential hazards, such as sinkholes or unstable slopes, allowing engineers to take proactive measures to mitigate risks.

Combining GPR with Artificial Intelligence (AI) offers a promising avenue for enhancing the accuracy and efficiency of subsurface investigations. Using AI algorithms, deep learning can give engineers and researchers deeper insights into subsurface features and properties. The development of Convolutional Neural Networks (CNN) has been instrumental in enabling deep learning to GPR interpretation. These networks are well suited for analyzing and interpreting complex datasets such as GPR data. By training AI models to learn from GPR data, researchers and engineers can benefit from accurate and detailed subsurface information, leading to the effective design and construction of geotechnical structures.

One of the major challenges in using AI for GPR data analysis is the lack of sufficiently large datasets to train and optimize deep learning models (Alzubaidi *et al.* 2023, Bansal *et al.* 2022). Deep learning algorithms are designed to learn patterns and features from many data without compromising performance and accuracy. The scarcity of big data in GPR analysis is attributed to several factors, including the high cost of GPR data collection, the limited availability of GPR survey sites, and the difficulty in obtaining ground-truth information that can be used to train and validate deep learning models. Consequently, researchers often rely on relatively small and heterogeneous datasets, leading to overfitting, poor generalization, and poor prediction accuracy. Table 1 lists the sizes of the

---

*Corresponding author, Professor
E-mail: geotech@hongik.ac.kr
[a]Doctoral Student
[b]Doctoral Student

ISSN: 2005-307X (Print), 2092-6219 (Online)

Table 1 The number of GPR datasets used for training AI algorithms for GPR interpretation

| Application field | Total number of data for AI model | | Applied data augmentation | Reference |
|---|---|---|---|---|
| | Number of real data | Number of generated data | | |
| Concrete building | 231 and 296 for each case | 0 | N/A | (Xiang *et al.* 2021) |
| Tunnel | 220 | 120 (synthesized) | GAN | (Qin *et al.* 2021) |
| Bridge and root | 188 | 0 | N/A | (Hou *et al.* 2021) |
| Highway | 90 | 748 (simulated)<br>5,866 (augmented) | numerical analysis geometry transformation | (Lei *et al.* 2019) |
| Road with underground pipeline | 187 | 1,683 (augmented) | geometry transformation | (Gao *et al.* 2021) |
| Concrete building | - | 3,992 (augmented) | geometry transformation | (Liu *et al.* 2020) |
| N/A | 0 | 900 (simulated) | numerical analysis | (Pasolli *et al.* 2009) |
| N/A | 100 | 100 (simulated) | numerical analysis | (Pham and Lefèvre 2018) |

datasets used to train the AI for GPR interpretation from previous studies. GPR datasets were manipulated by adopting simulated, synthesized, and augmented datasets referring to data created using numerical analysis, new data synthesized using an algorithm such as Generative Adversarial Networks (GAN), and data obtained by applying the data augmentation technique that only consider geometry transformations, respectively.

The study presented in Table 1 has two limitations: (1) Despite efforts to increase the amount of training data, the generated data still appears to be insufficient for general deep learning training. The following paragraphs describe the amount of data needed for typical deep learning training. (2) Although there are many different data augmentation techniques, only geometric transformations are used, and clean data is often employed through numerical analysis, resulting in data that is very different from actual GPR data being used for model training.

Larger datasets create better deep learning models (Halevy *et al.* 2009, Sun *et al.* 2017). Data-augmentation techniques can be employed to overcome these shortcomings of GPR data by increasing the number of datasets. Data augmentation has been widely used in other fields, including skin lesion classification (Esteva *et al.* 2017), liver lesion classification (Frid-Adar *et al.* 2018), cancer classification (Chaudhari *et al.* 2020), melanoma diagnosis (Kato *et al.* 2020), tomato leaf disease identification (Wu *et al.* 2020), CIFAR-10 image classification (Gu *et al.* 2019), plant disease diagnosis (Cap *et al.* 2020), global forecasting model (Bandara *et al.* 2021), and animal audio classification (Nanni *et al.* 2020). In the studies above, advancements in AI models were confirmed using data augmentation techniques. The number of augmented datasets implemented in these studies was contingent on the number of original datasets, with augmented datasets ranging from several thousand to more than 70,000 being created as a general rule.

The primary objective of this study is to acquire a sufficient dataset using various data augmentation techniques and to investigate the effectiveness of various types of data augmentation techniques in the context of GPR data analysis. One of the limitations of previous research is the lack of sufficient training data, which constrains the performance of AI models. Another limitation is that even when data augmentation was employed, only a limited range of methods, such as geometric transformations and numerical analyses, were utilized. In this study, we aimed to address these two limitations by actively introducing a variety of data augmentation techniques. Given the effectiveness of data augmentation techniques across various fields, we applied four distinct data augmentation techniques to GPR B-scan data. To facilitate transfer learning, the augmented dataset was fed into a pre-trained model, all layers of the pre-trained model were retrained for GPR B-scan analysis, and a new deep learning model was developed. The enhanced models, combined with GPR detection tasks and AI models, will significantly improve the accuracy and speed of GPR applications in civil engineering.

## 2. Backgrounds

### *2.1 Principle of GPR*

It is important to know the characteristics of EM waves to understand GPR. As shown in Fig. 1(a), GPR works by emitting high-frequency EM waves into a medium, receiving the reflected waves from a target, locating the target, and evaluating its properties. Because the propagation speed of EM waves in air is equal to the speed of light, the target's distance can be calculated from the round-trip time of the EM waves. These waves are partially reflected at the interface between different layers with different properties commonly represented by the dielectric constant. Some are transmitted through the next layer, continuing to propagate. The propagation speed and wavelength of the EM wave depend on the dielectric constant of each layer through which the EM wave passes. Therefore, if the layer's dielectric constant and the EM wave's travel time are available, the interface between layers, objects' presence, and locations can be evaluated. To understand and analyze the characteristics of GPR data, one must be familiar with A-scans and B-scans. An A-scan is a

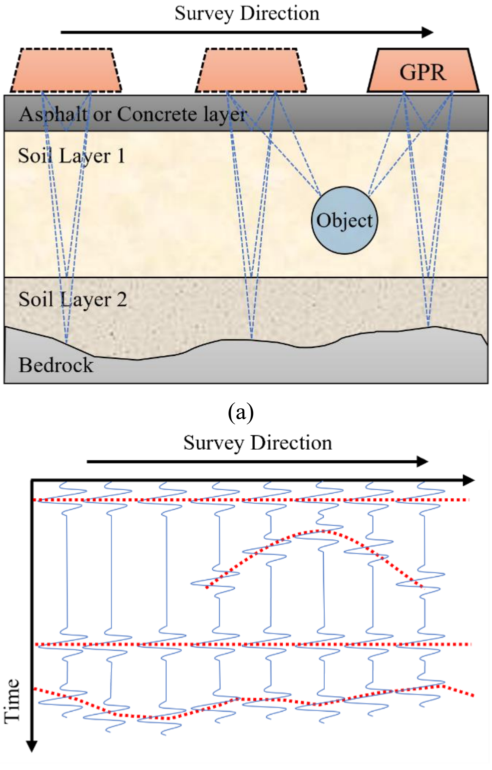

Fig. 1 Principle of GPR: (a) Penetration and reflection in the layer of the EM wave emitted from the transmitter and (b) B-scan data through A-scan data

one-dimensional data set of reflected EM waves recorded by a receiver, including information on the amplitude and round-trip time of the wave. The B-scan shown in Fig. 1(b) is a two-dimensional dataset created by organizing the A-scan data in the direction of the survey.

### 2.2 Data augmentation

By converting the amplitude of each EM wave in Fig. 1(b) into a color scale, the resulting visualization is shown in Fig. 2(a). The GPR B-Scan data can exhibit variations in color and scale depending on the user's application. If the wavelength in Fig. 2(a) is magnified by the same ratio, it may appear that the edges in Fig. 2(b) are further enhanced. Modifying the color scale of this data once more results in a different color distribution, as depicted in Fig. 3(c). Additionally, if the user opts to zoom in on a specific area, the scale may change accordingly, as illustrated in Fig. 4(d). It should also be noted that due to the nature of electromagnetic waves, noise may be introduced during the data acquisition process. When developing an object detection AI model for GPR B-Scan, it is crucial to consider these factors and appropriately build the training dataset.

Data augmentation technique refers to a method of expanding a dataset by making minor changes while retaining the core characteristics of the data. It is also commonly used when converging geotechnical engineering and artificial intelligence technology (Abdelmawla *et al.* 2023, Lee *et al.* 2022). In this study, considering the aforementioned characteristics of the GPR B-Scan data, we employed geometric transformations, color-space transformations, noise injection, and kernel filtering as data augmentation techniques for the experiment.

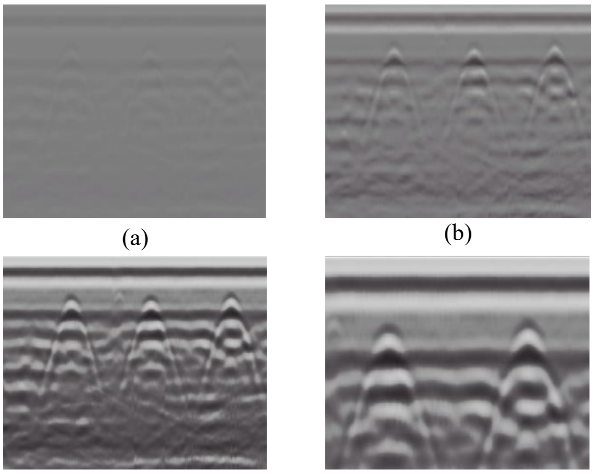
(a) (b)
(c) (d)

Fig. 2 GPR B-Scan images observed in various ways depending on the user environment: (a) Image without preprocessing, (b) Image with clearly visible edges by amplifying amplitude, (c) Image with changed color distribution, and (d) Image with magnified area of interest

One common approach is geometric transformation, which includes operations like scaling, translation, rotation, reflection, and shearing. These transformations are relatively simple yet can significantly enhance the performance of AI models by providing diverse data representations. Another important technique is color-space transformation, which involves converting an image from one color space to another. In deep learning, color spaces are mathematical models representing colors with numerical values. Common color spaces include RGB (Red, Green, Blue), HSV (Hue, Saturation, Value). By manipulating these color channels, adjustments can be made to brightness, saturation, and hue, thereby overcoming lighting challenges and improving image quality. Noise injection is also a popular technique, used to simulate noisy images by adding random values from distributions such as Gaussian, impulse, or speckle noise to the image matrix. This technique helps in making models more robust by exposing them to a variety of noise conditions. Lastly, applying kernel filters, or masks, to images is a method used to modify features. These filters, which are typically small matrices like 3×3 or 5×5, slide across an image, updating pixel values based on the weighted sum of the pixels within the kernel's coverage area. Common filters include those for edge detection, sharpening, and embossing, each of which enhances specific attributes of the images.

## 3. Deep learning models

The open-source TensorFlow Object Detection API (Application Programming Interface) framework facilitates

Table 2 Comparison of features of Faster R-CNN ResNet, SSD ResNet, and EfficientDet

| Feature | Faster R-CNN ResNet | SSD ResNet | EfficientDet |
|---|---|---|---|
| Speed | Medium | Fast | Very fast |
| Accuracy | High | Moderate | High |
| Structure | Two-stage (RPN + Object Detection) | Single-stage (SSD) | Single-stage with BiFPN |
| Backbone | ResNet-50, ResNet-101 | ResNet-50, ResNet-101 | EfficientNet |
| Model Size/ Computational Cost | Large | Medium | Small (Efficient) |
| Key Advantages | High accuracy, precise object localization | Fast speed, suitable for real-time detection | High accuracy and speed, efficient model size, scalability |
| Drawbacks | Slow inference speed, high computational cost | Relatively lower accuracy, weaker small object detection | Complex model design, requires tuning |
| Core Technologies | Region Proposal Network (RPN), RoI Pooling | Default Boxes, Multi-scale Feature Maps | BiFPN, Compound Scaling, |
| Scalability | Vertical scalability (can use deeper backbone networks) | Horizontal scalability (can add more default boxes) | Both horizontal and vertical scalability (can scale based on EfficientNet backbone) |

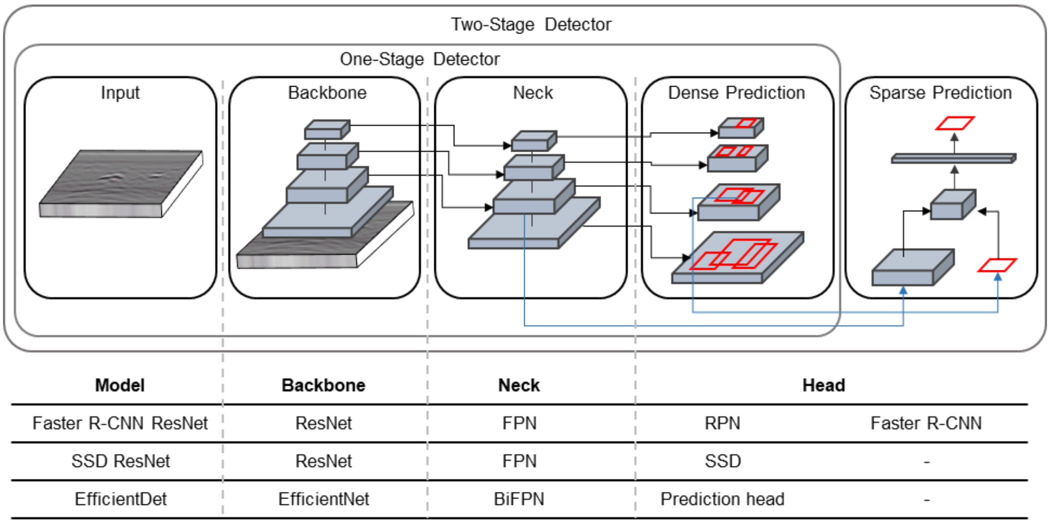

| Model | Backbone | Neck | Head | |
|---|---|---|---|---|
| Faster R-CNN ResNet | ResNet | FPN | RPN | Faster R-CNN |
| SSD ResNet | ResNet | FPN | SSD | - |
| EfficientDet | EfficientNet | BiFPN | Prediction head | - |

Fig. 3 Comparison of architectures of Faster R-CNN ResNet, SSD ResNet, and EfficientDet

the development of object-detection models. This study leveraged three architecture of models: faster region-based convolutional neural network with a residual network (Faster R-CNN ResNet), and single-shot multi-box detector (SSD) ResNet, scalable and efficient object detection (EfficientDet). The characteristics of the three models have been tabulated (Table 2) and the structural differences have been visualized (Fig. 3). The key features and architectures of each model are explained in the subsequent paragraphs.

### *3.1 Faster R-CNN ResNet*

The Faster R-CNN ResNet was developed by combining the Faster R-CNN (Ren *et al.* 2015) and ResNet (He *et al.* 2016) as the backbone network for improved object detection. Faster R-CNN ResNet employs a two-stage structure. In the first stage, a Region Proposal Network (RPN) generates potential object locations. In the second stage, these proposals are classified and their boundaries are refined. The model typically uses ResNet-50 or ResNet-101 as the backbone network, offering superior feature extraction capabilities. This structure results in very high accuracy and precise object localization. However, it also means that the model has a slower inference speed and higher computational costs, making it less suitable for real-time applications. Faster R-CNN ResNet is ideal for applications that demand high accuracy, and it can achieve vertical scalability by utilizing deeper backbone networks.

### *3.2 SSD ResNet*

The SSD ResNet, based on the SSD algorithm (Liu *et al.* 2016), is known for its ability to detect objects using feature maps of different sizes without requiring additional training processes. SSD ResNet features a single-stage structure, performing object classification and bounding box prediction in one forward pass through the network. It uses ResNet-50 or ResNet-101 as the backbone network, providing a good balance of performance. The model is

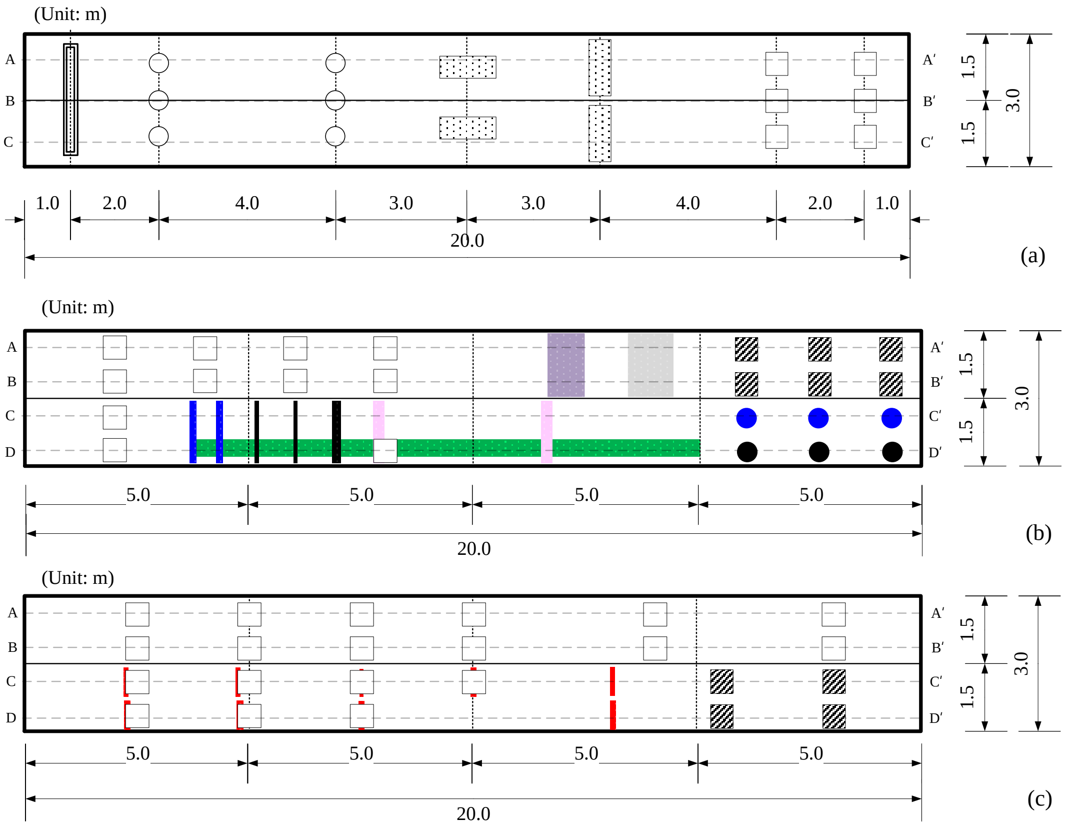

Fig. 5 Plan view of underground buried structures: (a) Section 1, (b) Section 2, and (c) Section 3

Fig. 4 A whole view of the test bed for GPR testing

known for its fast detection speed, making it suitable for real-time applications. However, it has relatively lower accuracy compared to two-stage detectors and struggles with detecting small objects. SSD ResNet allows for horizontal scalability by adding more default boxes, effectively handling objects of various sizes.

### 3.3 EfficientDet

EfficientDet utilizes a single-stage detection model with a Bidirectional Feature Pyramid Network (BiFPN) for efficient feature fusion. It employs EfficientNet (Tan and Le 2019) as the backbone network, which is known for balancing accuracy and efficiency. This model offers high accuracy and speed while maintaining an efficient model size and computational cost. One of the key advantages of EfficientDet is its compound scaling capability, which simultaneously adjusts resolution, depth, and width for superior scalability. Despite its complex design requiring careful tuning, EfficientDet excels in handling objects of different sizes and is highly efficient.

## 4. Methodology

### 4.1 Test site

Fig. 4 shows the bird-view testing site for the GPR scanning used in this study, located in Gapyeong, Gyeonggi, South Korea. Sections 1 and 2 contain asphalt pavement, and section 3 contains concrete pavement. The number on the pavement is the number of the three sections, each with a different pavement type and underground condition. Fig. 5 shows a detailed plan view of the underground buried structures with dimensions. Each section was 3 m wide and 20 m long, and various objects and cavities were formed at various locations. Other information, such as the types, shapes, lengths, and buried depths of the cavity models and objects, is confidential because the site is being used to verify the GPR performance. Still, non-disclosed information does not compromise the scope of this study. The total number of scanlines across Section 1, which comprises three scanlines (A-A', B-B', C-C'), and Sections 2 and 3, which each contain four scanlines (A-A', B-B', C-C', D-D'), summing up total eleven different scanlines.

Table 4 Description of the dataset for each case

| Case | | Descriptions |
|---|---|---|
| Real data | 1 (Reference) | Preprocessing real datasets for training |
| Generated data by data augmentation | 2 (Geometry) | Shift randomly -20 ~ 20 pixels in the x- and y-axis directions<br>Scaling randomly 80 ~ 100%<br>Flipping vertically |
| | 3 (Color space) | Randomly change values for brightness, hue, saturation, and hue and saturation between 70 and 130% |
| | 4 (Noise) | Add Gaussian, Shot, Impulse, and Speckle noises |
| | 5 (Kernel filter) | Convolve each image with a 3x3 kernel<br>Sharpen an image, then overlay the results with the original<br>Emboss an image, then overlay the results with the original<br>Detect edges in images, then overlay these with the original |

Table 3 Specification of GPR equipment.

| System | | Value |
|---|---|---|
| Manufacturer | | GSSI |
| Typical Range | | 6 m |
| Maximum Range | | 10 m |
| Frequency | | 350 MHz |
| Precision | Horizontal | 8 mm |
| | Vertical | 4 mm |
| Scan Speed | | 250 scans/sec |
| Remark | | Hyper stacking |

### *4.2 Data acquisition*

Table 3 presents the specifications of the GPR equipment used in this study. The frequency of the transmitted EM waves was 350 MHz, and the device could measure depths of up to 10 m, but with a typical measurement depth of 6 m. The precision of the GPR equipment was 8 and 4 mm in the horizontal (scanline) and vertical (depth) directions, respectively.

Each scan line was scanned 10 times, and the total number of scanlines measured by the GPR equipment was 110. The number of real data for AI training was 2,714, obtained through preprocessing of 110 scanline data as follows: In the first step, the raw data from scanlines were adjusted using a gain function in the commercial software RADAN7 (GSSI 2017). The gain function is essential in optimizing the analysis of GPR signals by adjusting the signal strength based on the arrival time. The GPR signal amplitude is usually too large at shallow depths without a gain function. It drops rapidly with depth, making evaluating the conditions at deeper depths challenging. Amplifying the signal at greater depths using the gain function enables the observation of the reflected wave at greater depths, which may not be observable without the gain function. The second step involves cropping the hyperbola in all the GPR B-scan data, indicators of buried objects, and 2,714 images were cropped for the experiments. To unify the input data size of the cropped images, they were trimmed to a specific size centered on the object of interest (hyperbola). The size used in this study was 640 × 640 pixels.

These preprocessing steps are essential for GPR B-scan data, as they amplify signal strength for deeper targets through the application of a gain function and isolate objects of interest via hyperbola cropping prior to the implementation of data augmentation techniques.

### *4.3 Data augmentation*

Data augmentation artificially alters data to increase the amount of available data, as described in Section 2. This technique is beneficial for image data, owing to its representation as a three-channel tensor. The preprocessed real dataset serves as a reference and is labeled as ‘Case 1’.

The real data of 2,714 preprocessed images were divided into a training dataset (2,172 images, 80%) and a testing dataset (542 images, 20%). The use of data augmentation can prevent overfitting by expanding the amount of data and becomes increasingly important when obtaining field and experimental data (i.e., GPR scan data).

The training dataset for Case 1 was augmented to 15,204 (7-fold) for each method using four different data augmentation techniques. The four augmented datasets were labeled Cases 2–5. Case 2 adopted a geometric transformation, including 1) translations ranging from -20 to +20 pixels along the x- and y-axes, 2) random scaling from 80% to 100% of the original image, and 3) vertical flipping. Case 3 utilized color space transformation by modifying the hue, saturation, and value (HSV) components, forming three image data channels. There are two prevalent approaches to computer image recognition: the RGB and HSV models. The RGB model represents color as a combination of red, green, and blue components, whereas the HSV model expresses color using hue, saturation, and value components. We randomly modified the original images' lightness, hue, and saturation between 70% and 130%. Case 4 adopted the noise injection technique, which can be achieved by artificially adding noise to images. The noise types include Gaussian, Shot, Impulse, and Speckle. Finally, Case 5 used a kernel filter by generating a particular type of kernel tensor or by using an algorithm to extract feature points from the image, which are then utilized to obtain tensors such as sharpen, emboss, and edge detection. Table 4 summarizes the data augmentation techniques and explanations applied to the datasets of cases 1 to 5 described above.

Fig. 6 shows examples of B-scan data from scanline,

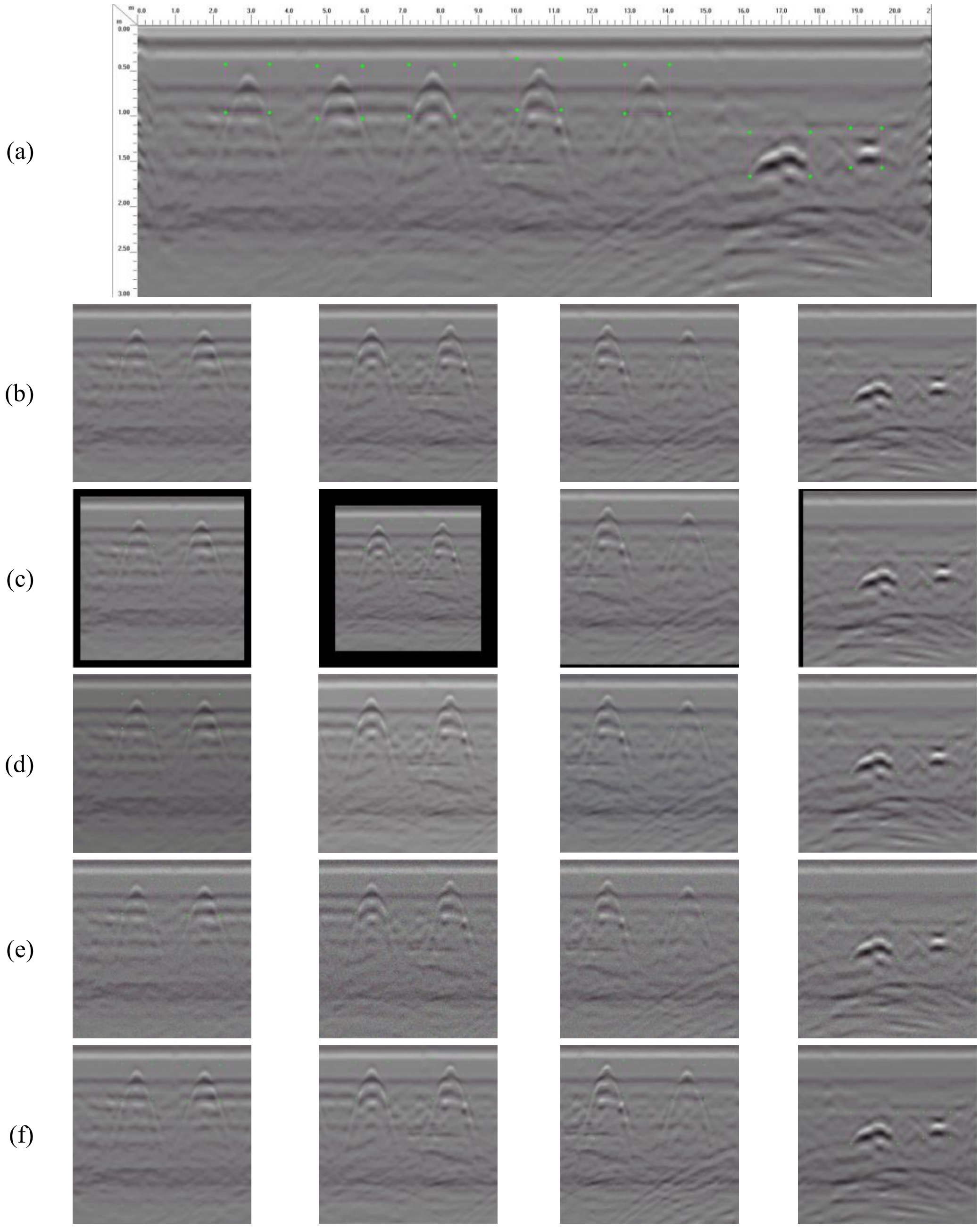

Fig. 6 Representative examples of each case: (a) Raw data from scanline, (b) Case 1 & Preprocessed real data,(c) Case 2 & Geometric deformation, (d) Case 3 & Color space transformation, (e) Case 4 & Applying noise, (f) Case 5 & Kernel filter

preprocessed real data (Case 1), and augmented data (Cases 2–5) with four different data augmentation techniques according to the entire data preparation process. Fig. 6(a) shows the scanline data obtained from the GPR analysis software before the preprocessing step. Fig. 6(b) shows the cropped images with a size of 640 × 640 pixels for training, and Fig. 6(c)-6(f) demonstrates the application of four data augmentation techniques: geometry, color space, noise, and kernel. In deep learning training, annotating the ground truth or correct answers is necessary through a labelling step. As illustrated in Fig. 6, the ground truth is indicated by a box represented by the coordinates of the four green dots. This study created a dataset with a class labelled as 'object,' where all ground truths were categorized as follows.

Fig. 7 presents an overview of the dataset preparation used for training and testing. Case 1 consisted of 2,714 preprocessed real images randomly divided into training and test sets. We manipulated a training set with 2,172 images to 15,204 images via data augmentation. The dataset used for testing was not used for data augmentation to eliminate any favorable effects on the algorithm's accuracy. The effectiveness of these data augmentation techniques will be evaluated by comparing the mean Average Precision (mAP) and Average Recall (AR) values obtained by

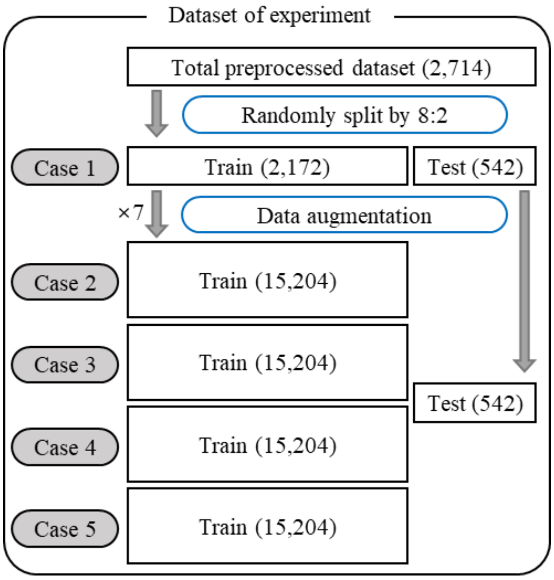

Fig. 7 Procedure of dataset preparation

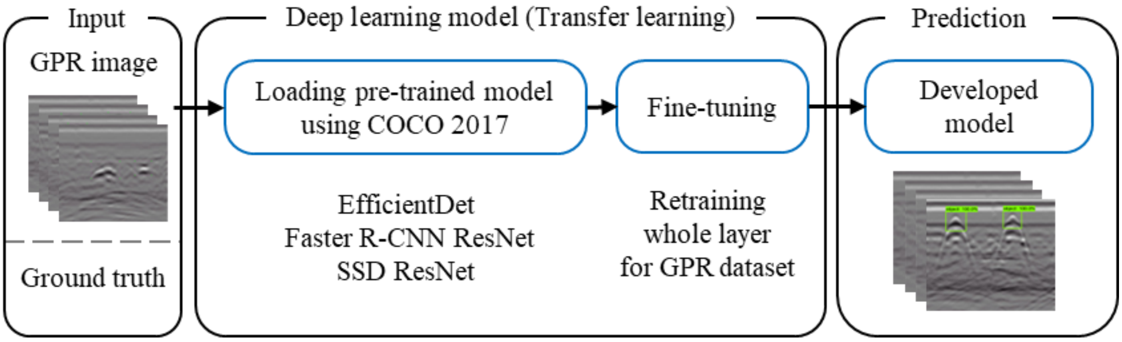

Fig. 8 Architecture of the deep learning model employing transfer learning for the GPR dataset

developed models trained on augmented datasets (Cases 2-5) with those of the baseline model trained on the real data set (Case 1).

### 4.4 Transfer learning

The programming language used was Python 3.6, and the framework used was TensorFlow 2.2. To summarize the workstation setup, we used 8,704 (4,352 × 2) CUDA cores, and CUDA 10.1 and cuDNN 7.6 for the GPU-accelerated library were installed to match the CUDA performance of the RTX 2080 Ti equipped on the workstation. Fig. 8 outlines the training process of the deep learning model. First, we curated five case datasets according to the procedures described in Section 4.3. The dataset for each case included GPR images and the ground truth as information for training. The base model was created by loading pre-trained models such as EfficientDet, Faster R-CNN ResNet, and SSD ResNet from the TensorFlow Object Detection API, using the COCO 2017 dataset (Lin *et al.* 2014). To create a new model for this study, the pre-trained model was transferred to the GPR B-scan dataset and fine-tuned appropriately. In the fine-tuning process, the weights of all layers of the loaded models were updated to enable better detection of the GPR dataset. By retraining the entire architecture in this way, we developed new object detection models for the GPR B-scan data sets of five cases.

### 4.5 Quantitative performance metrics

We evaluated the developed models using mAP and AR, commonly used metrics for object detection in computer vision. The mAP and AR are performance evaluation indices for the (Common Object in Context) metric. They provide indices to represent the performance of an object detection model (Everingham *et al.* 2010). It is necessary to understand the confusion matrix to evaluate the performance of the developed models in deep learning. Fig. 9 shows the confusion matrix that determines the states (TP, FP, FN, and TN) according to the actual and predicted values. This matrix calculates evaluation indices such as precision, recall, mAP, and AR.

The precision and recall are defined by Eqs. (1) and (2), respectively.

$$Precision = \frac{TP}{TP + FP} = \frac{TP}{all\ detections} \tag{1}$$

| | | Predicted | |
|---|---|---|---|
| | | Positive | Negative |
| Actual | Positive | **TP** | **FN** |
| | Negative | **FP** | **TN** |

Fig. 9 Confusion matrix

$$Recall = \frac{TP}{TP + FN} = \frac{TP}{all\ ground\ truths} \qquad (2)$$

Precision measures the number of positive cases predicted as true, which is the ratio of true positive cases to the total number of predicted positives. Precision indicates a measure of a model's ability to avoid false positives. Recall is a measure of a model's ability to avoid false negatives. The recall measures the number of positive cases correctly identified by a model, which is the ratio of true-positive cases to the total number of positive cases.

The mAP and AR can be calculated from the precision and recall results. The mAP is a commonly used metric for evaluating the performance of object-detection algorithms measuring the model's accuracy in localizing and classifying objects in an image. We calculated the mAP by taking each class's average precision (AP) across different confidence thresholds. The AP measures the precision-recall curve of the model for each class. We calculated the AR by taking the average recall of each class across the different levels of overlap thresholds. Recall measures the number of true positives identified by the model out of all the ground truth objects.

The mAP and AR results vary based on the Intersection over Union (IoU) metric threshold. For object detection, it is necessary to establish a criterion to determine whether the prediction result is positive or negative. The most commonly used criterion is the IoU, which can be expressed as the ratio of the overlap and union of the prediction box and ground truth (Fig. 10). The higher the IoU value, the more accurate the prediction box is concerning the ground truth. We evaluated the model using the following four metrics: AP50, AP75, AP, and AR, and calculated them for different IoU threshold values. AP50, AP75, and AP are the values determined for mAP when the IoU thresholds were 0.5, 0.75, and 0.5:0.95 at 0.5 intervals, respectively. In other words, the AP is the average mAP calculated with IoU thresholds ranging from 0.5 to 0.95. This can be considered a higher criterion than the AP50 and AP75. The IoU threshold used to calculate the AR was 0.5:0.95, as in the AP.

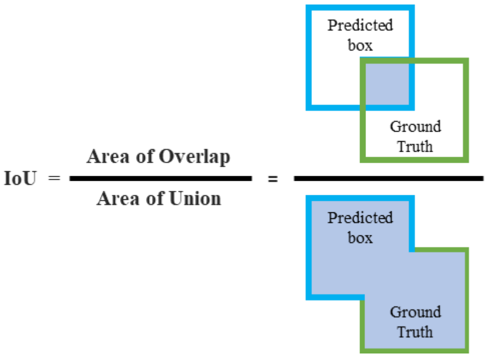

Fig. 10 Concept of Intersection over Union (IoU)

## 5. Results and discussion

### 5.1 Performance evaluation

Table 5 summarizes the three developed models' mAPs at different IoU and AR values. The improvements in mAP and AR vary significantly depending on the developed model and the selected IoU thresholds; however, both mAP and AR increased effectively by adopting data augmentation in all cases. In particular, the improvement was considerable for AP75, AP, and AR for EfficientDet and SSD ResNet. In contrast, a relatively small improvement was observed for Faster R-CNN ResNet because the model predicted well regardless of IoU and data augmentation. AP75 for the Faster R-CNN ResNet without data augmentation (Case 1) was 98.8, resulting in a slight improvement after applying data augmentation. On the other hand, those for EfficientDet and SSD ResNet were 63.1 and 62.9, respectively, which were improved to values ranging from 94.2 to 97.9 after data augmentation. The improvements were minimal for an IoU of 50 (AP50) because the values were already near unity without data augmentation.

Figs. 11 and 12 show the AP and AR for comparing the models and data augmentation techniques. As shown in Fig. 11, both the EfficientDet and the SSD ResNet exhibited a significant increase in the AP, ranging from 36.3 to 39.7%, and the Faster R-CNN ResNet exhibited a slight improvement of only 4.4 to 6.3% after the data augmentation techniques. We observed similar trends for the AR, with a substantial increase rate of 24.9 to 34.9% for the EfficientDet and the SSD ResNet and a small increase rate of 4.1 to 5.1% for the Faster R-CNN ResNet.

An intriguing observation is that the Faster R-CNN ResNet model, despite its excellent baseline performance, exhibited relatively small improvements when data augmentation techniques were applied. This trend does not suggest that data augmentation techniques lack a significant impact on Faster R-CNN. Notably, in the Faster R-CNN ResNet model, both mAP and AR achieved the highest results with the application of data augmentation techniques. Increasing AR necessitates the model to detect as many real-world objects as possible, primarily focusing on reducing false negatives (missed detections). This process is likely to increase false positives. However, an increase in mAP was also observed. To achieve a higher mAP, the model must reduce both false positives (incorrect detections) and false negatives (missed detections). Therefore, the Faster R-CNN ResNet model, demonstrating increases in both mAP and AR, can be considered optimized with higher accuracy and comprehensive detection capabilities.

Table 5 mAP and AR according to data augmentation technique

| Data type | Model | mAP (Mean Average Precision) | | | AR (Average Recall) |
|---|---|---|---|---|---|
| | | AP50 | AP75 | AP | AR |
| Case 1 (reference) | EfficientDet | 96.0 | 63.1 | 56.2 | 65.1 |
| | Faster R-CNN ResNet | 100.0 | 98.8 | 82.3 | 86.1 |
| | SSD ResNet | 95.5 | 62.9 | 56.9 | 65.3 |
| Case 2 (Geometric) | EfficientDet | 100.0 | 96.8 | 76.6 | 81.3 |
| | Faster R-CNN ResNet | 100.0 | 99.0 | 87.5 | 90.1 |
| | SSD ResNet | 98.4 | 94.2 | 78.7 | 83.0 |
| Case 3 (Color space) | EfficientDet | 100.0 | 97.9 | 78.4 | 83.1 |
| | Faster R-CNN ResNet | 100.0 | 98.8 | 85.9 | 89.6 |
| | SSD ResNet | 99.7 | 97.9 | 84.1 | 88.1 |
| Case 4 (Noise) | EfficientDet | 100.0 | 97.4 | 78.4 | 83.0 |
| | Faster R-CNN ResNet | 100.0 | 98.9 | 87.5 | 90.5 |
| | SSD ResNet | 97.7 | 94.7 | 78.6 | 86.3 |
| Case 5 (Kernel) | EfficientDet | 100.0 | 97.1 | 78.5 | 82.9 |
| | Faster R-CNN ResNet | 100.0 | 99.0 | 86.4 | 89.8 |
| | SSD ResNet | 99.8 | 96.4 | 79.5 | 83.4 |

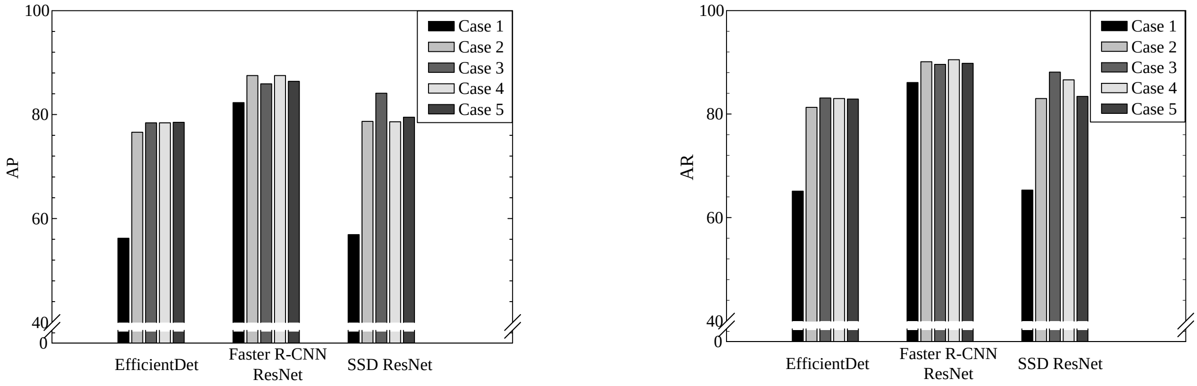

(a) Average Precision (b) Average Recall

Fig. 11 AP (mAP @ IoU = 0.5:0.95) and AR (AR @ IoU = 0.5:0.95) for the three models: (a) Average precision, and (b) Average recall

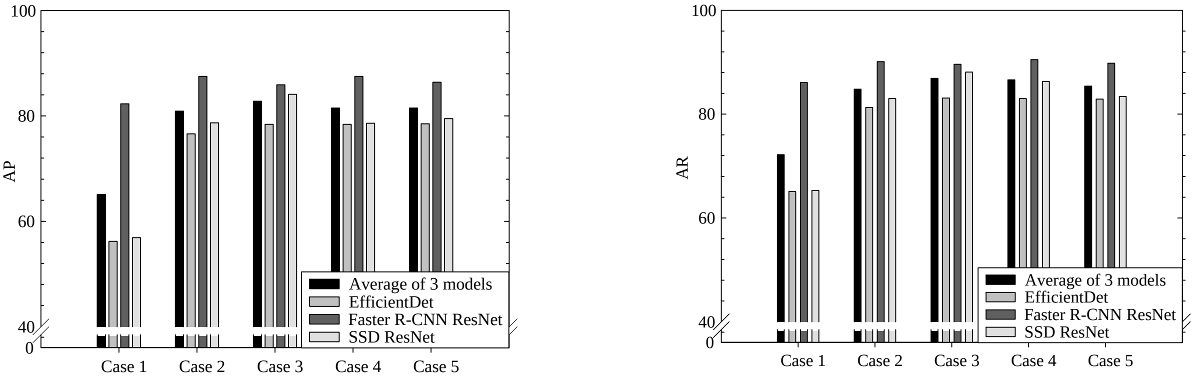

(a) Average Precision (b) Average Recall

Fig. 12 AP (mAP @ IoU = 0.5:0.95) and AR (AR @ IoU = 0.5:0.95) for the five cases: (a) Average precision, and (b) Average recall

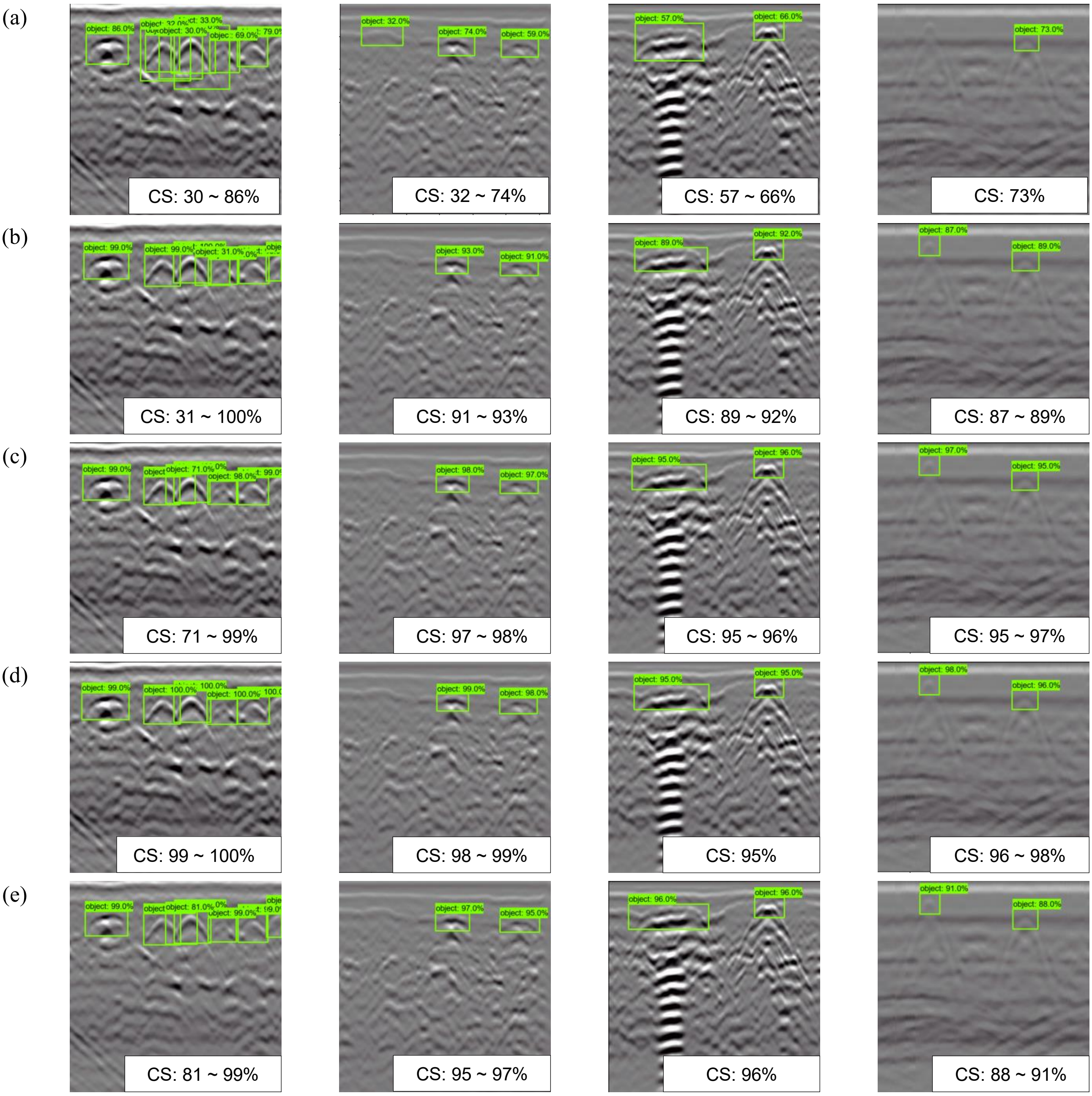

Fig. 13 Representative examples of object detection in GPR B-scan using EffcientDet: (a) Case 1, (b) Case 2, (c) Case 3, (d) Case 4, and (e) Case 5 (note: CS refers to Confidence Score).

Among the three models compared in this study, Faster R-CNN utilizes a two-stage architecture and has a relatively large number of parameters, which can be advantageous for recognizing complex patterns. Consequently, although it requires more computational resources, Faster R-CNN can

Among the three models compared in this study, Faster R-CNN utilizes a two-stage architecture and has a relatively large number of parameters, which can be advantageous for recognizing complex patterns. Consequently, although it requires more computational resources, Faster R-CNN can

### *5.2 Object detection*

Figs. 13-15 show representative examples of object detection in GPR B-scan data using the three models, respectively. We randomly extracted the examples from images with obvious improvements. Each figure includes the detected GPR hyperbolas with the confidence scores of four different B-scan images. By the definitions of mAP and AR, the mAP is related to the false detection of the models, and the AR to the detection miss in the image data. The Faster R-CNN ResNet model, the best performing model in terms of mAP and AR, displays precise detection with high confidence scores regardless of the data augmentation techniques.

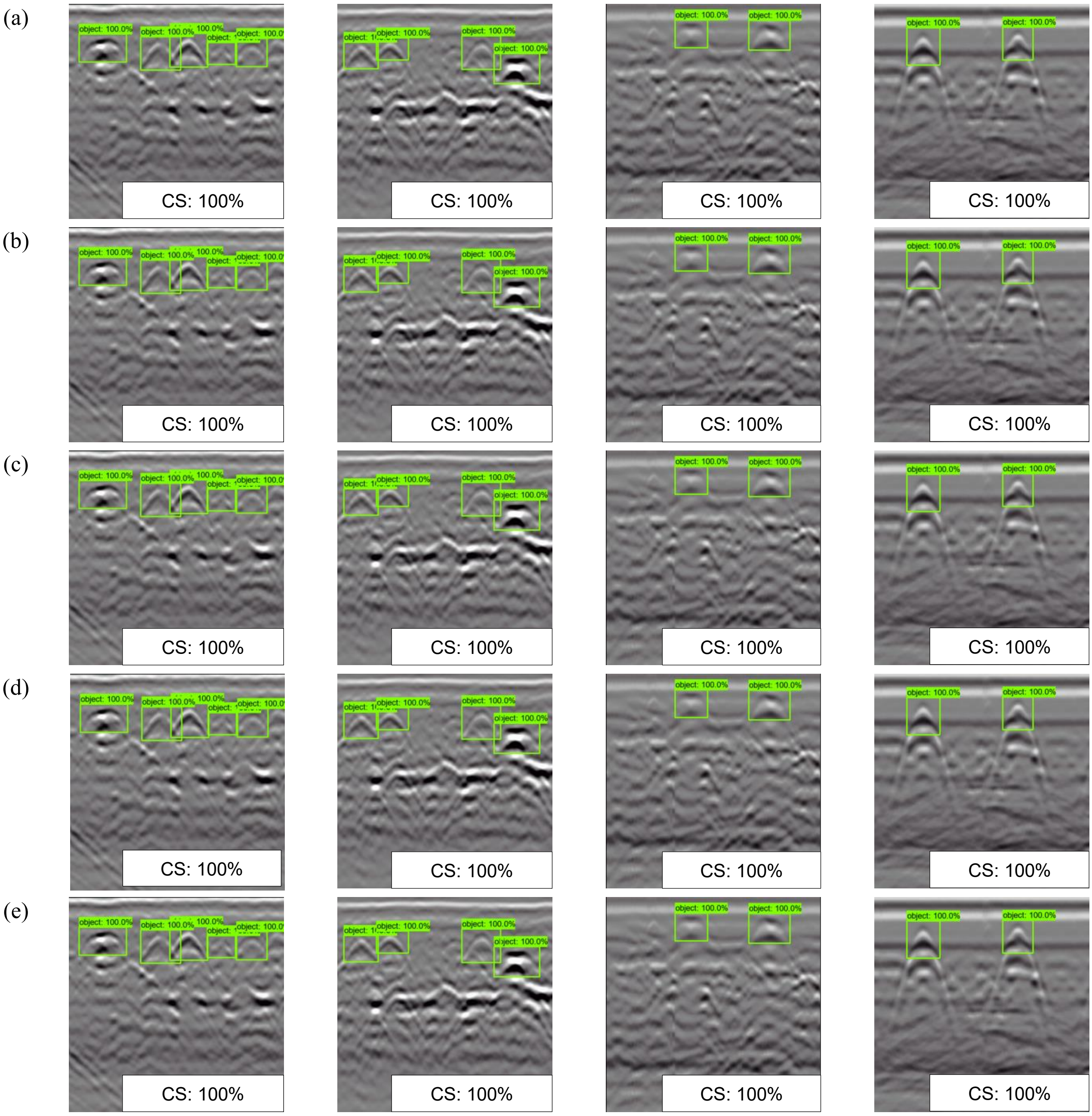

Fig. 14 Representative examples of object detection in GPR B-scan using Faster R-CNN ResNet: (a) Case 1, (b) Case 2, (c) Case 3, (d) Case 4, and (e) Case 5 (note: CS refers to Confidence Score)

On the contrary, we found the EfficientDet and SSD ResNet to either miss detection or incorrectly detect without data augmentation (refer to Figs. 13-15). For example, Fig. 13 indicates that the EfficientDet detects too many hyperbolas, which are not the ground truths before data augmentation, but it correctly detects them after data augmentation. The right figure of Fig. 13(a) shows an example of a missing detection, which is also corrected after data augmentation. Similar improvements in object detection were observed for the SSD ResNet, as shown in Fig. 15. It is interesting to note that the confidence scores in objection detection are higher in the figures for Cases 2-5 since the mAP metric is positively related to the confidence score.

From a geotechnical and safety perspective, it is beneficial to develop models that prioritize increasing the AR. A high AR indicates that most true positives are detected, resulting in fewer missed detections, which is crucial because missing an object (false-negative) can have serious consequences. In contrast, the incorrect detection of objects (false-positive) is less critical, as long as the number is not excessive, because these can be filtered out more easily. Additionally, in GPR object detection, high AR is From a geotechnical and safety perspective, it is beneficial

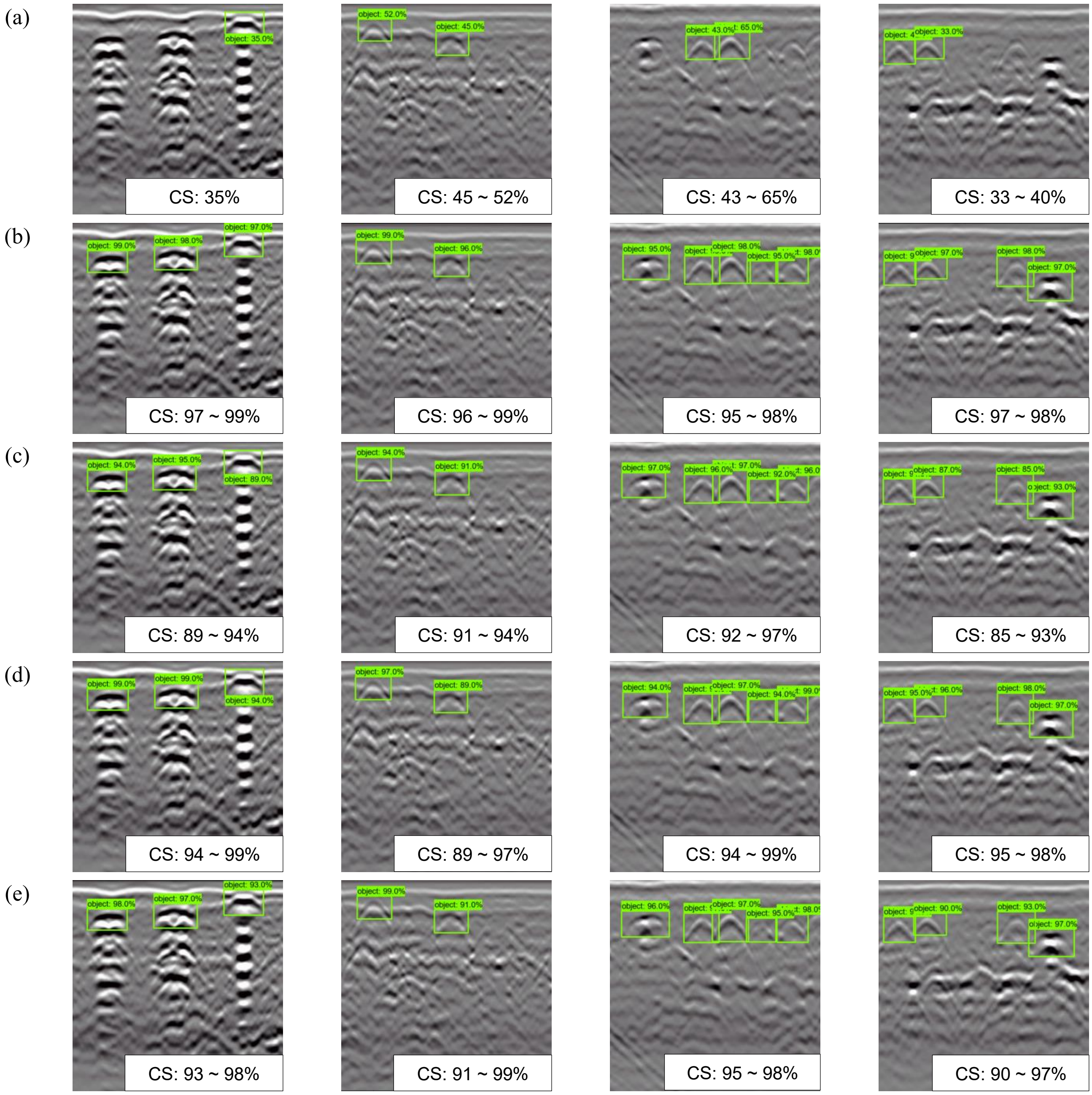

Fig. 15 Representative examples of object detection in GPR B-scan using SSD ResNet: (a) Case 1, (b) Case 2, (c) Case 3, (d) Case 4, and (e) Case 5 (note: CS refers to Confidence Score).

to develop models that prioritize increasing the AR. A high AR indicates that most true positives are detected, resulting in fewer missed detections, which is crucial because missing an object (false-negative) can have serious consequences. In contrast, the incorrect detection of objects (false-positive) is less critical, as long as the number is not excessive, because these can be filtered out more easily. Additionally, in GPR object detection, high AR is essential for identifying critical subsurface features, such as utilities or voids, which, if missed, could lead to significant structural or safety hazards.

## 6. Conclusions

This study evaluates the effectiveness of data augmentation techniques for object detection using GPR B-scan data. GPR B-scan images were obtained from 110 scanlines in the testbed with various buried objects, resulting in the real data of 2,714 preprocessed images containing hyperbolas. We divided the preprocessed dataset into training and test sets at a ratio of 8:2, and 2,172 training images were considered the reference training set (Case 1). We generated four training sets (Cases 2–5) using four different data augmentation techniques, resulting in 15,204 training images per set. In this study, we adopted three pre-trained models (EfficientDet, Faster R-CNN ResNet, and SSD ResNet) and used five different training datasets to develop the new models for GPR B-scan dataset. We used the mAP and AR metrics to evaluate the performance of the three developed models before and after data augmentation. The following conclusions were drawn:

- Improvements in mAP and AR varied depending on the selected IoU threshold; however, it is clear that, in most cases, data augmentation techniques enhanced both mAP and AR. In particular, the improvements were significant for EfficientDet and SSD ResNet. However, the improvement was minor for the Faster R-CNN ResNet.
- The increases in AP and AR range from 36.3 to 39.7% and from 24.9 to 34.9%, respectively, for the EfficientDet and SSD ResNet with data augmentation techniques. The increase for the Faster R-CNN ResNet was approximately 5.0% because the values of the model were sufficiently high, even before the data augmentation.
- The developed models (three models for five cases) were used to detect objects in the GPR B-scan data. EfficientDet and SSD ResNet presented higher confidence scores and better performance in object detection after data augmentation.
- Because the Faster R-CNN ResNet showed higher mAP and AR before data augmentation, the model showed good object detection with high confidence scores, regardless of the data augmentation technique. Faster R-CNN ResNet outperformed the others, due to its two-stage architecture and extensive parameters, which aid in recognizing complex patterns.
- The AR metric seems more significant than the mAP metric because false negatives in object detection may result in serious consequences. The application of data augmentation techniques led to improvements in the AR metric, indicating that this technique is highly beneficial for creating training images for object detection in GPR B scans.

This study demonstrates the effectiveness of data augmentation for GPR B-scan object detection. However, this research is limited by the use of a single test site and a specific set of buried objects. Future research should involve testing these methods on a larger dataset with more diverse GPR data and exploring more sophisticated data augmentation techniques. Furthermore, while the conclusions primarily address the technical contributions, it is crucial to emphasize the broader applicability of the findings. These results hold significant potential for the development of robust GPR object detection systems, which can be invaluable for various applications such as identifying buried utilities, locating potential sinkholes, and characterizing underground structures.

## Declaration of competing interest

The authors declare that they have no conflicts of interest that could have appeared to influence the work reported in this paper.

## Acknowledgments

This work was supported by the National Research Foundation of Korea (NRF) grant funded by the Korea government (MSIT) (No. 2023R1A2C1007635), partly supported by 2024 Hongik University Innovation Support Program Fund.

## References

Abdelmawla, A., Ma, S., Yang, J.J. and Kim, S.S. (2023), “Subsurface anomaly detection utilizing synthetic GPR images and deep learning model”, *Geomech. Eng.*, **33**(2), 203-209. https://doi.org/10.12989/gae.2023.33.2.203.

Alani, A.M. and Tosti, F. (2018), “GPR applications in structural detailing of a major tunnel using different frequency antenna systems”, *Constr. Build. Mater.*, **158**, 1111-1122. https://doi.org/10.1016/j.conbuildmat.2017.09.100.

Alzubaidi, L., Bai, J., Al-Sabaawi, A., Santamaría, J., Albahri, A., Al-dabbagh, B.S.N., Fadhel, M.A., Manoufali, M., Zhang, J., and Al-Timemy, A.H. (2023), “A survey on deep learning tools dealing with data scarcity: definitions, challenges, solutions, tips, and applications”, *J. Big Data*, **10**(1), 1-82. https://doi.org/10.1186/s40537-023-00727-2.

Baker, G.S., Jordan, T.E., Pardy, J., Baker, G.S. and Jol, H.M. (2007), An introduction to ground penetrating radar (GPR). *Stratigraphic Analyses Using GPR*, Geological Society of America.

Bandara, K., Hewamalage, H., Liu, Y.H., Kang, Y. and Bergmeir, C. (2021), “Improving the accuracy of global forecasting models using time series data augmentation”, *Pattern Recognition*, **120**, 108148. https://doi.org/10.1016/j.patcog.2021.108148.

Bansal, M.A., Sharma, D.R. and Kathuria, D.M. (2022), “A systematic review on data scarcity problem in deep learning: solution and applications”, *ACM Computing Surveys (CSUR)*, **54**(10), 1-29. https://doi.org/10.1145/3502287.

Benedetto, A. (2013), “A three dimensional approach for tracking cracks in bridges using GPR”, *J. Appl. Geophys.*, **97**, 37-44. https://doi.org/10.1016/j.jappgeo.2012.12.010.

Benedetto, A., Manacorda, G., Simi, A. and Tosti, F. (2012), “Novel perspectives in bridges inspection using GPR”, *Nondestruct. Test. Eval.*, **27**(3), 239-251. https://doi.org/10.1080/10589759.2012.694883.

Cap, Q.H., Uga, H., Kagiwada, S. and Iyatomi, H. (2020), “Leafgan: An effective data augmentation method for practical plant disease diagnosis”, *IEEE T. Automat. Sci. Eng.*, **19**(2), 1258-1267. https://doi.org/10.1109/TASE.2020.3041499.

Çelik, E. (2015), “Investigation of the underground structure elements of GSM towers with GPR and GSM signal effects in GPR data”, *Proceedings of the 2015 8th International Workshop on Advanced Ground Penetrating Radar (IWAGPR)*, IEEE.

Chaudhari, P., Agrawal, H. and Kotecha, K. (2020), “Data augmentation using MG-GAN for improved cancer classification on gene expression data”, *Soft Comput.*, **24**, 11381-11391. https://doi.org/10.1007/s00500-019-04602-2.

Chun, P.J., Suzuki, M. and Kato, Y. (2023), “Iterative application of generative adversarial networks for improved buried pipe detection from images obtained by ground-penetrating radar”, *Comput.-Aided Civil Infrastruct. Eng.*, **38**(17), 2472-2490.

Esteva, A., Kuprel, B., Novoa, R.A., Ko, J., Swetter, S.M., Blau, H.M. and Thrun, S. (2017), “Dermatologist-level classification of skin cancer with deep neural networks”, *Nature*, **542**(7639), 115-118. https://doi.org/10.1038/nature21056.

Everingham, M., Van Gool, L., Williams, C.K., Winn, J. and

Zisserman, A. (2010), "The pascal visual object classes (voc) challenge", *Int. J. Comput. Vision*, **88**, 303-338.

Feng, D., Wang, X. and Zhang, B. (2018), "Specific evaluation of tunnel lining multi-defects by all-refined GPR simulation method using hybrid algorithm of FETD and FDTD", *Constr. Build. Mater.*, **185**, 220-229. https://doi.org/10.1016/j.conbuildmat.2018.07.039.

Frid-Adar, M., Diamant, I., Klang, E., Amitai, M., Goldberger, J. and Greenspan, H. (2018), "GAN-based synthetic medical image augmentation for increased CNN performance in liver lesion classification", *Neurocomputing*, **321**, 321-331. https://doi.org/10.1016/j.neucom.2018.09.013.

Gao, Y., Pei, L., Wang, S. and Li, W. (2021), "Intelligent detection of urban road underground targets by using ground penetrating radar based on deep learning", *J. Physi.: Conf. Ser.*, 1757, 012081. https://doi.org/10.1088/1742-6596/1757/1/012081.

GSSI (2017), "RADAN 7 manual", GSSI Nashua, NH.

Gu, S., Pednekar, M. and Slater, R. (2019), "Improve image classification using data augmentation and neural networks", *SMU Data Science Review*, **2**(2), 1.

Halevy, A., Norvig, P. and Pereira, F. (2009), "The unreasonable effectiveness of data", *IEEE Intell. Syst.*, **24**(2), 8-12. https://doi.org/10.1109/MIS.2009.36.

He, K., Zhang, X., Ren, S. and Sun, J. (2016), "Deep residual learning for image recognition", *Proceedings of the IEEE conference on computer vision and pattern recognition*.

Hou, F., Lei, W., Li, S. and Xi, J. (2021), "Deep learning-based subsurface target detection from GPR scans", *IEEE Sensor. J.*, **21**(6), 8161-8171. https://doi.org/10.1109/JSEN.2021.3050262.

Kato, K., Nemoto, M., Kimura, Y., Kiyohara, Y., Koga, H., Yamazaki, N., Christensen, G., Ingvar, C., Nielsen, K. and Nakamura, A. (2020), "Performance improvement of automated melanoma diagnosis system by data augmentation", *Adv. Biomed. Eng.*, **9**, 62-70. https://doi.org/10.14326/abe.9.62.

Kong, S.M., Kim, D.M., Lee, D.Y., Jung, H.S. and Lee, Y.J. (2018), "Field and laboratory assessment of ground subsidence induced by underground cavity under the sewer pipe", *Geomech. Eng.*, **16**(3), 285-293. https://doi.org/10.12989/gae.2018.16.3.285.

Köprücü, F., Erer, I. and Kumlu, D. "Clutter aware deep detection for subsurface radar targets", *Proceedings of the 2021 IEEE International Geoscience and Remote Sensing Symposium IGARSS*, IEEE.

Kouros, G., Kotavelis, I., Skartados, E., Giakoumis, D., Tzovaras, D., Simi, A. and Manacorda, G. (2018), "3d underground mapping with a mobile robot and a gpr antenna", *Proceedings of the 2018 IEEE/RSJ International Conference on Intelligent Robots and Systems (IROS)*, IEEE.

Lai, W.W., Chang, R.K. and Sham, J.F. (2017), "Detection and imaging of city's underground void by GPR", *Proceedings of the 2017 9th International Workshop on Advanced Ground Penetrating Radar (IWAGPR)*, IEEE.

Lee, H.L., Song, K.I., Qi, C. and Kim, K.Y. (2022), "Sequential prediction of TBM penetration rate using a gradient boosted regression tree during tunneling", *Geomech. Eng.*, **29**(5), 523-533. https://doi.org/10.12989/gae.2022.29.5.523.

Lei, W., Hou, F., Xi, J., Tan, Q., Xu, M., Jiang, X., Liu, G. and Gu, Q. (2019), "Automatic hyperbola detection and fitting in GPR B-scan image", *Automati. Constr.*, **106**, 102839. https://doi.org/10.1016/j.autcon.2019.102839.

Lin, C., Wang, X., Li, Y., Zhang, F., Xu, Z. and Du, Y. (2020), "Forward modelling and GPR imaging in leakage detection and grouting evaluation in tunnel lining", *KSCE J. Civil Eng.*, **24**, 278-294. https://doi.org/10.1007/s12205-020-1530-z.

Lin, T.Y., Maire, M., Belongie, S., Hays, J., Perona, P., Ramanan, D., Dollár, P. and Zitnick, C.L. (2014), "Microsoft coco: Common objects in context", *Proceedings of the Computer Vision–ECCV 2014: 13th European Conference, Zurich, Switzerland, September 6-12, 2014, Proceedings, Part V 13*, Springer.

Liu, H., Lin, C., Cui, J., Fan, L., Xie, X. and Spencer, B.F. (2020), "Detection and localization of rebar in concrete by deep learning using ground penetrating radar", *Automat. Constr.*, **118**, 103279. https://doi.org/10.1016/j.autcon.2020.103279.

Liu, W., Anguelov, D., Erhan, D., Szegedy, C., Reed, S., Fu, C.Y. and Berg, A.C. (2016), "Ssd: Single shot multibox detector", *Proceedings of the Computer Vision–ECCV 2016: 14th European Conference, Amsterdam, The Netherlands, October 11-14, 2016, Proceedings, Part I 14*, Springer.

Liu, Z., Han, K., Xue, K., Song, Y., Liu, L., Tang, Y. and Zhu, Y. (2022), "Improving CT-image universal lesion detection with comprehensive data and feature enhancements", *Multimedia Syst.*, **28**(5), 1741-1752.

Luo, T.X. and Lai, W.W. (2020), "GPR pattern recognition of shallow subsurface air voids", *Tunn. Undergr. Sp. Tech.*, **99**, 103355. https://doi.org/10.1016/j.tust.2020.103355.

Nanni, L., Maguolo, G. and Paci, M. (2020), "Data augmentation approaches for improving animal audio classification", *Ecol. Inform.*, **57**, 101084. https://doi.org/10.1016/j.ecoinf.2020.101084.

Pasolli, E., Melgani, F. and Donelli, M. (2009), "Automatic analysis of GPR images: A pattern-recognition approach", *IEEE T. Geosci. Remote Sens.*, **47**(7), 2206-2217. https://doi.org/10.1109/TGRS.2009.2012701.

Persico, R. (2014), *Introduction to ground penetrating radar: inverse scattering and data processing*, John Wiley & Sons.

Pham, M.T. and Lefèvre, S. (2018), "Buried object detection from B-scan ground penetrating radar data using Faster-RCNN", *Proceedings of the IGARSS 2018-2018 IEEE international geoscience and remote sensing symposium*, IEEE.

Qin, H., Zhang, D., Tang, Y. and Wang, Y. (2021), "Automatic recognition of tunnel lining elements from GPR images using deep convolutional networks with data augmentation", *Automat. Constr.*, **130**, 103830. https://doi.org/10.1016/j.autcon.2021.103830.

Ren, S., He, K., Girshick, R. and Sun, J. (2015), "Faster r-cnn: Towards real-time object detection with region proposal networks", *Adv. Neural Inform. Process. Syst.*, **28**.

Sun, C., Shrivastava, A., Singh, S. and Gupta, A. (2017), "Revisiting unreasonable effectiveness of data in deep learning era", *Proceedings of the IEEE international conference on computer vision*.

Tallini, M., Giamberardino, A., Ranalli, D. and Scozzafava, M. (2004), "GPR survey for investigation in building foundations", *Proceedings of the 10th International Conference on Grounds Penetrating Radar, 2004. GPR 2004.*, IEEE.

Tan, M. and Le, Q. (2019), "Efficientnet: Rethinking model scaling for convolutional neural networks", *Proceedings of the International conference on machine learning*, PMLR.

Tanoli, W.A., Sharafat, A., Park, J. and Seo, J.W. (2019), "Damage Prevention for underground utilities using machine guidance", *Automat. Constr.*, **107**, 102893. https://doi.org/10.1016/j.autcon.2019.102893.

Traoré, A., Ly, A.O. and Akhloufi, M.A. (2020), "Evaluating deep learning algorithms in pulmonary nodule detection", *Proceedings of the 2020 42nd Annual International Conference of the IEEE Engineering in Medicine & Biology Society (EMBC)*, IEEE.

Utsi, E.C. (2017), *Ground penetrating radar: theory and practice*, Butterworth-Heinemann, United Kingdom, Oxford.

Wu, Q., Chen, Y. and Meng, J. (2020), "DCGAN-based data augmentation for tomato leaf disease identification", *IEEE Access*, **8**, 98716-98728.

https://doi.org/10.1109/ACCESS.2020.2997001.

Xiang, Z., Ou, G. and Rashidi, A. (2021), “Automated translation of rebar information from GPR data into as-built BIM: A deep learning-based approach”, *Comput. Civil Eng., 2021*, 374-381.

Yang, H., Liu, Y., Li, Y., Pan, R., Wang, H., Luo, F., Wang, H. and Cao, S. (2020), “Research on the support of larger broken gateway based on the combined arch theory”, *Geomech. Eng.*, **23**(2), 93-102. https://doi.org/10.12989/gae.2020.23.2.093.

Yang, Y., Lu, J., Li, R., Zhao, W. and Yan, D. (2020), “Small-scale void-size determination in reinforced concrete using GPR”, *Adv. Civil Eng.*, **2020**, 1-11. https://doi.org/10.1155/2020/2740309.

Yuan, C., Li, S., Cai, H. and Kamat, V. R. (2018), “GPR signature detection and decomposition for mapping buried utilities with complex spatial configuration”, *J. Comput. Civil Eng.*, **32**(4), 04018026. https://doi.org/10.1061/(ASCE)CP.1943-5487.0000764.

*IC*